Zhong et al. EURASIP Journal on Advances in Signal Processing (2017) 2017:33
DOI 10.1186/s13634-017-0470-3

EURASIP Journal on Advances in Signal Processing

RESEARCH Open Access

Focusing high-squint and large-baseline one-stationary bistatic SAR data using keystone transform and enhanced nonlinear chirp scaling based on an ellipse model

Hua Zhong*, Song Zhang, Jian Hu and Minhong Sun

Abstract

This paper deals with the imaging problem for one-stationary bistatic synthetic aperture radar (BiSAR) with high-squint, large-baseline configuration. In this bistatic configuration, accurate focusing of BiSAR data is a difficult issue due to the relatively large range cell migration (RCM), severe range-azimuth coupling, and inherent azimuth-geometric variance. To circumvent these issues, an enhanced azimuth nonlinear chirp scaling (NLCS) algorithm based on an ellipse model is investigated in this paper. In the range processing, a method combining deramp operation and keystone transform (KT) is adopted to remove linear RCM completely and mitigate range-azimuth cross-coupling. In the azimuth focusing, an ellipse model is established to analyze and depict the characteristic of azimuth-variant Doppler phase. Based on the new model, an enhanced azimuth NLCS algorithm is derived to focus one-stationary BiSAR data. Simulating results exhibited at the end of this paper validate the effectiveness of the proposed algorithm.

Keywords: Bistatic synthetic aperture radar (BiSAR), One-stationary, Azimuth-variant, Keystone-transform (KT), Ellipse model, Nonlinear chirp scaling (NLCS)

1 Introduction

Bistatic synthetic aperture radar (BiSAR) system is operated with separated transmitter and receiver platforms which offers particular advantages like flexible configuration, reduced cost, strong hiding performance, and forward-looking imaging ability when it is compared with traditional monostatic SAR [1–5]. Owing to these benefits, BiSAR has raised increasing concerns in SAR research community in the last decade.

One-stationary BiSAR, where the transmitter or the receiver is stationary, is a special configuration of general BiSAR that is relatively easy to be constructed and deployed. This kind of BiSAR is of great value to remote sensing applications, as it allows small and light-weighted unmanned aerial vehicles or in-orbit SAR satellite to produce bistatic images [6, 7]. The one-stationary BiSAR could be used to image the target area and exploit multi-dimensional information, such as region monitoring, resolution enhancement, and ground moving target detection and imaging, which makes broad application prospects in both civilian and military fields [8, 9].

Currently, many imaging algorithms have been proposed for one-stationary BiSAR. In [10, 11], nonlinear chirp scaling (NLCS) algorithm has been applied to focus one-stationary BiSAR data, where a curve fitting method is used to generate a perturbation function to equalize the azimuth-variant frequency modulation (FM) rate. In [12–14], NLCS algorithm is combined with keystone transform (KT) to handle one-stationary BiSAR data. In these methods, KT is used to eliminate the linear range-azimuth coupling that increases with the squint angle, and then, numerical integral is utilized in

* Correspondence: zhonghbig@gmail.com
School of Communication Engineering, Hangzhou Dianzi University, Hangzhou 310018, China

the azimuth focusing to generate the perturbation function. Inverse scaled Fourier transform (ISFT) can also handle one-stationary BiSAR data [15, 16]. This kind of algorithm uses chirp multiplications and FFTs in the frequency domain to achieve the 2-D spatial variance correction which avoids the use of interpolation. Furthermore, omega-k algorithm is also applied to the image formation of one-stationary BiSAR [17, 18]. In this algorithm, 2-D Stolt transformation is used to deal with the spatial variance, but the Stolt interpolation makes the method quite time-consuming.

In summary, NLCS is an excellent algorithm proposed in recent years for image formation of one-stationary BiSAR, which was originally adopted for monostatic SAR to equalize the azimuth-variant Doppler FM rate [19]. In [20], this algorithm has been applied to focus BiSAR data. However, the inherent geometric variance of BiSAR has not been taken into account, and thus, the scene size of the final image is restricted. In [21], the NLCS has been extended for BiSAR with a model of range offset to improve the azimuth equalization. With the increase of baseline, however, the range offset model is becoming inaccurate, which leads to deterioration of the imaging performance. To overcome this issue, numerical methods for NLCS are utilized in [10–14] to generate the perturbation function, but these methods need a large amount of computation, and also, their applicability is limited.

In this paper, an ellipse model is established to reveal the azimuth-variant characteristic of slant ranges for BiSAR, and then, an enhanced NLCS algorithm based on the new model is proposed to focus one-stationary BiSAR data with high-squint, large-baseline configuration. In this algorithm, deramp operation is used first to remove the range walk and the Doppler ambiguity of the echo, and then, KT is utilized to eliminate the residual linear RCM. After that, bulk range cell migration correction (RCMC) and second range compression (SRC) are carried out to compensate the high-order RCM and range compression terms. Following that, an azimuth ellipse model is constructed to reveal the azimuth-variant characteristic of BiSAR. Based on the new model, an enhanced azimuth NLCS is derived to focus one-stationary BiSAR data at last.

The rest of this paper is organized as follows. Section 2 gives the geometric signal model of BiSAR with stationary transmitter. Section 3 presents the range processing by deramp operation, KT, and bulk RCMC. In Section 4, the azimuth-variant characteristic of BiSAR is analyzed based on a new azimuth model, and then, the enhanced azimuth NLCS is derived. Simulation results of the proposed algorithm are given in Section 5. Finally, conclusions are provided in Section 6.

2 Geometry and signal model

The geometry configuration of strip-map BiSAR with stationary transmitter is shown in Fig. 1. $P_0(x_0, y_0)$ is chosen as the scene center, and $P(x, y)$ is an arbitrary target in the imaging area. The receiver is flying along the y-axis with a constant velocity of v, and its original coordinate is (x_R, y_R, h_R). The coordinate of the stationary transmitter is (x_T, y_T, h_T).

The slant range history of the receiver with respect to the target $P(x, y)$ is

$$R_R(t; r_{Rc}, t_c) = \sqrt{r_{Rc}^2 + v^2(t-t_c)^2 - 2r_{Rc}v(t-t_c)sin(\theta_R)}$$
$$r_{Rc} = \sqrt{(x-x_R)^2 + (y-y_R)^2 + h_R^2} \tag{1}$$

where t is the azimuth slow time and r_{Rc} and θ_R represent the slant range and squint angle of the receiver at the beam center crossing time $t = t_c$, respectively. Differently, the range history of the stationary transmitter to target $P(x, y)$ is a constant one,

$$R_T = r_{Tc} = \sqrt{(x-x_T)^2 + (y-y_T)^2 + h_T^2}. \tag{2}$$

Then, the bistatic range history is the sum of $R_R(t; r_{Rc}, t_c)$ and R_T, which can be expanded into a Taylor series of t at $t = t_c$ for further analysis [14]

$$R_{\text{total}}(t; r_c, t_c) = R_R(t; r_{Rc}, t_c) + R_T$$
$$\approx Z_0 + A_0(t-t_c) + \frac{B_0}{2}(t-t_c)^2 + \frac{C_0}{6}(t-t_c)^3 \tag{3}$$

where $Z_0 = r_c = r_{Rc} + r_{Tc}$ denotes the bistatic slant range at $t = t_c$. A_0, B_0, and C_0 are the expanding coefficients and given by

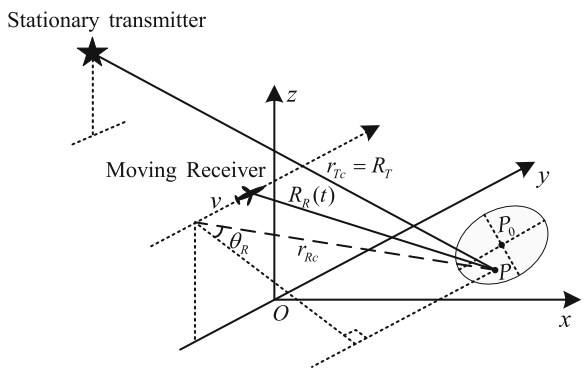

Fig. 1 The imaging geometry model of strip-map BiSAR with stationary transmitter

$$A_0 = -v\sin(\theta_R),\quad B_0 = \frac{v^2\cos^2(\theta_R)}{r_{Rc}},\quad C_0 = \frac{3v^3\cos^2(\theta_R)sin(\theta_R)^2}{r_{Rc}}. \tag{4}$$

For the subsequent description, (3) can be rewritten as

$$R_{\text{total}}(t;r_c,t_c) = Z_1(r_c,t_c) + A_1(r_c,t_c)t + \frac{B_1(r_c,t_c)}{2}t^2 + \frac{C_0}{6}t^3 \tag{5}$$

where

$$\begin{aligned} Z_1(r_c,t_c) &= Z_0 - A_0 t_c + \frac{B_0}{2}t_c^2 - \frac{C_0}{6}t_c^3 \\ A_1(r_c,t_c) &= A_0 - B_0 t_c + \frac{C_0}{2}t_c^2,\quad B_1(r_c,t_c) = B_0 - C_0 t_c \end{aligned} \tag{6}$$

The linear term in (5) represents the linear RCM, and the high-order terms represent the high-order RCMs, respectively.

Supposing the transmitted signal is a linear frequency modulated (LFM) signal, the received echo from $P(x, y)$ after being demodulated to baseband is

$$\begin{aligned} s(\tau,t;r_c,t_c) = {} & w_{\text{r}}\left(\tau - \frac{R_{\text{total}}(t;r_c,t_c)}{c}\right) w_{\text{a}}\left(\frac{t-t_c}{T_{\text{a}}}\right) \\ & \times exp\left\{-j2\pi f_{\text{c}}\frac{R_{\text{total}}(t;r_c;t_c)}{c}\right\} exp\left\{j\pi K_r\left[\tau - \frac{R_{\text{total}}(t;r_c,t_c)}{c}\right]^2\right\} \end{aligned} \tag{7}$$

where τ is the range fast time and $w_{\text{r}}(\cdot)$ and $w_{\text{a}}(\cdot)$ imply the range and azimuth envelopes, respectively. T_{a} is the synthetic aperture time, f_{c} is the carrier frequency, K_{r} is the range FM rate, and c represents the speed of light.

3 Range processing

In this section, we first quantitatively analyze the ratio of linear RCM component to high-order RCM components with varying squint angles to confirm that the linear RCM component dominates the total RCM in high-squint BiSAR. Then, based on that point, we used a method combining deramp operation and keystone transform to remove the linear RCM completely. In this method, deramp operation is utilized to eliminate the range walk and the Doppler ambiguity of the echo, and then, KT is used to remove the residual linear RCM left by deramp operation. After that, bulk RCMC and SRC are performed to compensate the high-order RCM and range compression terms. At last, analyses are conducted to validate the effectiveness of the range processing.

3.1 RCM proportion analysis

Taking the bistatic range history of the scene center as an example, the linear RCM and the high-order one in (5) can be expressed as

$$\begin{aligned} R_W(t;\theta_R) &= A_0(\theta_R)t \\ R_C(t;\theta_R) &= R_{\text{total}}(t;\theta_R) - A_0(\theta_R)t - r_{\text{cref}} \end{aligned} \tag{8}$$

where $R_{\text{total}}(t;\theta_R)$ denotes the bistatic range history of the scene center. Figure 2 gives the shape of $R_C(t;\theta_R)$ with varying squint angles from 0° to 70° based on BiSAR parameters in Table 1. It can be seen that the high-order RCM is becoming smaller as the squint angle is getting larger. To quantitatively analyze the ratio of the linear RCM to high-order one, we define

$$WCR(\theta_R) = Q_W(\theta_R)/Q_C(\theta_R), \tag{9}$$

where $Q_W(\theta_R)$ and $Q_C(\theta_R)$ imply the cumulative sums of the linear RCM and high-order one within a synthetic aperture time, respectively, and given by

$$Q_W(\theta_R) = \sum_{-T_a/2}^{T_a/2} R_W(t;\theta_R),\quad Q_C(\theta_R) = \sum_{-T_a/2}^{T_a/2} R_C(t;\theta_R). \tag{10}$$

Figure 3 shows the simulated result of $WCR(\theta_R)$ based on the same BiSAR parameters used in Fig. 2. It is obvious that the ratio is rapidly getting large with the increase of the squint angle, and it is even beyond 500 times when the squint angle is reaching 60°.

3.2 Algorithm derivation

Based on the discussion aforementioned, we can affirm that in high-squint BiSAR, the linear RCM component takes the dominant part of the total RCM, while the high-order RCM is extremely small. When the squint angle is approaching 70°, for instance, the high-order RCM at the edge in azimuth is only about 3.0 m, while the ratio of linear RCM to high-order one is over 1500 times. Accordingly, the linear RCMC operation is particularly significant in the entire RCMC for high-squint BiSAR. Once the linear RCM is removed, only a small

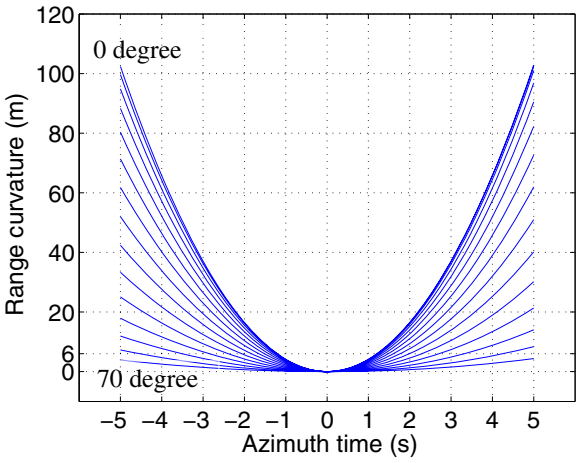

Fig. 2 High-order RCM with varying squint angles

Table 1 Stationary parameters of BiSAR

Simulation parameters	Transmitter	Receiver
Velocity		220 m/s
Beam center slant range	37.52 km	12.48 km
Squint angle		62°
Altitude	4.8 km	2.67 km
Pulse repetition frequency	208Hz	
Carrier frequency	10.0GHz	
Range bandwidth	75.0 MHz	
Synthetic aperture time	2.07 s	
Bistatic bsaeline range	32 km	

amount of high-order RCM will remain, and it is much easier to be corrected. Therefore, we apply the combination of deramp operation and KT to remove the linear RCM and then a bulk RCMC to correct the high-order RCM.

In summary, the RCMC operations in this paper contain three steps: deramp operation, keystone transform, and bulk RCMC. The processing results of these three steps on the echo are shown in Fig. 4, and the detailed algorithm will be discussed in the following.

Deramp operation is applied first, which is a common processing method in the range-frequency and azimuth-time domain. Before deramp operation, the echo (7) should be transformed into the range-frequency and azimuth-time domain by using the principle of stationary phase (PSP), and the signal is (the constant term ignored)

$$S(f_r,t;r_c,t_c)=exp\left(-j\pi\frac{f_r^2}{K_r}\right)exp\{-j2\pi\frac{f_r+f_c}{c}[Z_1(r_c,t_c)+A_1(r_c,t_c)t+\frac{B_1(r_c,t_c)}{2}t^2+\frac{C_0}{6}t^3]\} \tag{11}$$

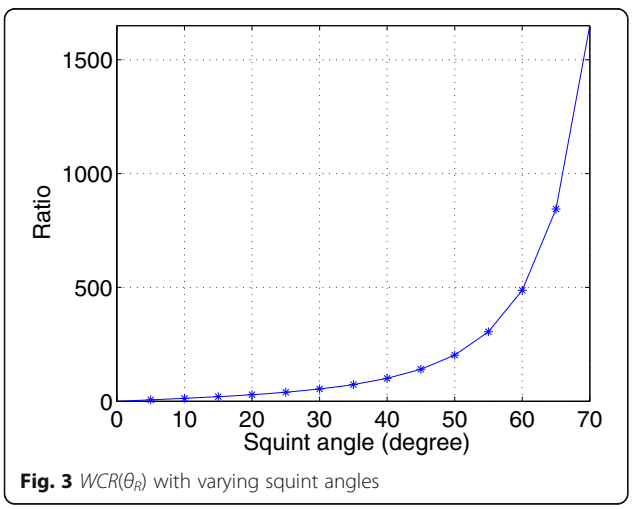

Fig. 3 *WCR*(θ_R) with varying squint angles

where f_r is the range frequency. Then, deramp operation is performed by constructing a filtering function at the azimuth center,

$$H_{\mathrm{Deramp}}(f_r,t)=exp\left\{j2\pi\frac{f_r+f_c}{c}A_0t\right\}. \tag{12}$$

Multiplying (12) with (11), we obtain

$$S_1(f_r,t;r_c,t_c)=exp\left(-j\pi\frac{f_r^2}{K_r}\right)exp\{-j2\pi\frac{f_r+f_c}{c}[Z_1(r_c,t_c)+\left(-B_0t_c+\frac{C_0}{2}t_c^2\right)t+\frac{B_1}{2}t^2+\frac{C_0}{6}t^3]\} \tag{13}$$

where B_1 is $B_1(r_c, t_c)$ for short. The bistatic range history after deramp operation becomes

$$R_{\mathrm{Deramp}}(t;r_c,t_c)=Z_1(r_c,t_c)+\left(-B_0t_c+\frac{C_0}{2}t_c^2\right)t+\frac{B_1}{2}t^2+\frac{C_0}{6}t^3. \tag{14}$$

In (14), the second term denotes the residual linear RCM and it is azimuth-variant. Thus, after deramp operation, only the linear RCMs of the central targets in azimuth have been fully removed, while the residual linear RCMs of the noncentral targets in azimuth still exist and cannot be ignored in high-squint BiSAR which will be discussed in Section 3.3.

Then, KT is performed to remove the residual linear RCMs of the noncentral targets in azimuth, which is essentially a resampling process along azimuth slow time [14]

$$t=\frac{f_c}{f_r+f_c}t_m \tag{15}$$

where t_m is the new azimuth slow time after KT.

Substituting (15) into (13) and expanding the result into a Taylor series of f_r at $f_r = 0$, we have

$$\begin{aligned}S_2(f_r,t_m;r_c,t_c)&=\exp\{j\varphi(f_r,t_m;r_c,t_c)\}\\&=\exp\{j[\varphi_0(t_m;r_c,t_c)+\varphi_1(t_m;r_c,t_c)f_r\\&\quad+\varphi_2(t_m;r_c,t_c)f_r^2+\sum_{n=3}^{\infty}\varphi_n(t_m;r_c,t_c)f_r^n]\}\end{aligned} \tag{16}$$

where

$$\begin{cases}\varphi_0(t_m;r_c,t_c)=-\frac{2\pi f_c}{c}\left[Z_1(r_c,t_c)+\left(-B_0t_c+\frac{C_0}{2}t_c^2\right)t_m+\frac{B_1}{2}t_m^2+\frac{C_0}{6}t_m^3\right]\\ \varphi_1(t_m;r_c,t_c)=-\frac{2\pi}{c}\left[Z_1(r_c,t_c)-\frac{B_1}{2}t_m^2-\frac{C_0}{3}t_m^3\right]\\ \varphi_2(t_m;r_c,t_c)=-\pi\left(\frac{1}{K_r}+\frac{B_1}{cf_c}t_m^2+\frac{C_0}{cf_c}t_m^3\right)\\ \varphi_n(t_m;r_c,t_c)=\frac{1}{n!}\frac{\partial^n\varphi(t_m,f_r;r_c,t_c)}{\partial f_r^n}\end{cases} \tag{17}$$

In (16), φ_0 is the azimuth modulation term, φ_1 is the range position term, and φ_2 and φ_n denote the SRC and high-order range-azimuth coupling terms, respectively.

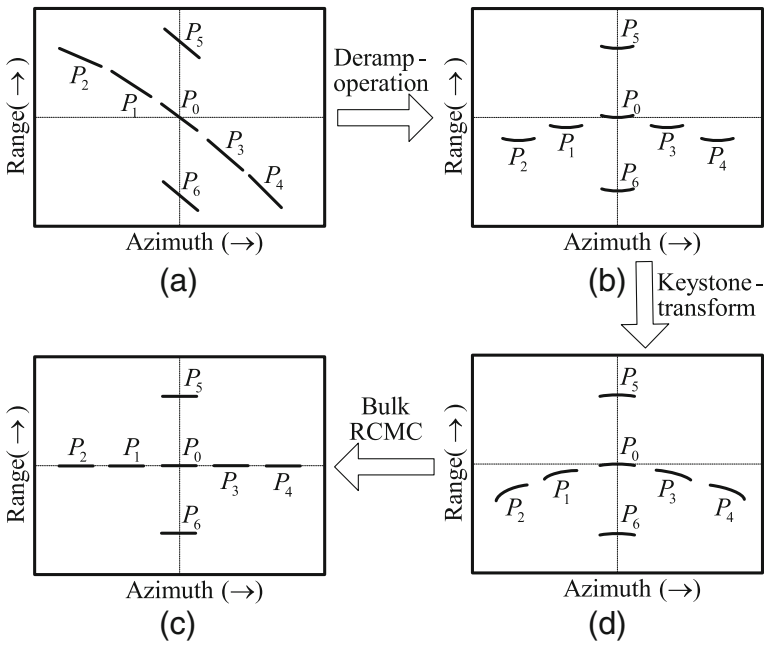

Fig. 4 Steps of RCMC (suppose the range compression has been performed). **a** Data space. P_0, P_1, P_2, P_3, and P_4 have the same bistatic slant ranges when azimuth time $t = 0$. P_0, P_5, and P_6 are in the same azimuth cell. **b** Data space after deramp operation. The ramps have been removed, but only the linear RCM of P_0 has been completely removed. **c** Data space after KT. Linear RCMs of all targets are removed. **d** Data space after bulk RCMC. RCMs of all targets are removed, and also, their range histories have been shifted into the same range cell

Inspecting φ_1, the linear term of t_m that is the linear RCM component has been fully removed after KT, which also greatly decreases the range-azimuth coupling. Therefore, the bistatic range history after KT becomes

$$R_{\mathrm{KT}}(t_m; r_c, t_c) = Z_1(r_c, t_c) - \frac{B_1}{2}t_m^2 - \frac{C_0}{3}t_m^3, \tag{18}$$

where the second and third terms imply the new high-order RCM after KT. To eliminate this new high-order RCM, we construct the bulk RCMC filtering function at the scene center as follows

$$H_{\mathrm{BRCMC}}(f_r, t_m; r_{cref}, 0) = exp\left\{-j\frac{2\pi}{c}\left(\frac{B_1(r_{cref}, 0)}{2}t_m^2 + \frac{C_0(r_{cref})}{3}t_m^3\right)f_r\right\}. \tag{19}$$

Multiplying (19) with (16), the bistatic range history after bulk RCMC becomes

$$R_{\mathrm{BRCMC}}(t_m; r_c, t_c) = Z_1(r_c, t_c) + \Delta Z_1, \tag{20}$$

where ΔZ_1 denotes the migration error caused by bulk RCMC. In high-squint BiSAR, this error is extremely small and can be neglected; the detailed analysis is given in Section 3.3.

If ΔZ_1 is ignored, the bistatic range history after bulk RCMC can be rewritten as

$$\begin{aligned} R_{\mathrm{BRCMC}}(t_m; r_c, t_c) &\approx Z_1(r_c, t_c) \\ &= Z_0 - A_0 t_c + \frac{B_0}{2}t_c^2 - \frac{C_0}{6}t_c^3 \\ &= R_{\mathrm{total}}(0; r_c, t_c) \end{aligned} \tag{21}$$

Comparing (21) with (5), the bistatic range history of target $P(x, y)$ has been shifted from original $R_{\mathrm{total}}(t; r_c, t_c)$ into the range cell at $R_{\mathrm{total}}(0; r_c, t_c)$ after RCMC. This effect can be expressed as follows

$$R_{\mathrm{total}}(t; r_c, t_c) \overset{\mathrm{RCMC}}{\rightarrow} R_{\mathrm{total}}(0; r_c, t_c). \tag{22}$$

Thus, we draw a conclusion that the bistatic range histories of echoes with the same $R_{\mathrm{total}}(0; r_c, t_c)$ in the coordinate plane have been shifted into a same range cell after RCMC.

Furthermore, the SRC and high-order coupling terms in (16) can also be compensated by constructing filtering functions at the scene center,

$$H_{\mathrm{SRC}}(f_r, t_m; r_{cref}, 0) = exp\left\{j\pi\left(\frac{1}{K_r} + \frac{B_1(r_{cref}, 0)}{cf_c}t_m^2 + \frac{C_0(r_{cref})}{cf_c}t_m^3\right)f_r^2\right\} \tag{23}$$

$$H_{\mathrm{HI}}(f_r, t_m; r_{cref}, 0) = exp\{j\varphi_3(t_m; r_{cref}, 0)f_r^3 \quad\} \tag{24}$$

where the high-order filter is usually kept up to third-order term.

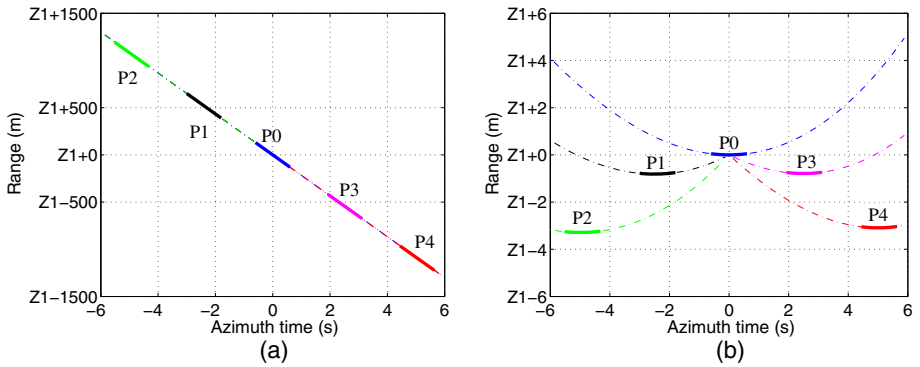

Fig. 5 Bistatic range histories of the echoes. **a** Before deramp operation. **b** After deramp operation ($Z_1 = R_{\text{total}}(0; r_c, t_c) = 50$ km)

After bulk RCMC and SRC, only the azimuth modulation term φ_0 in (16) remains. Then, transforming the signal into azimuth frequency domain using PSP, we obtain

$$S_3(f_a; r_c, t_c) = exp\{j\varphi_0(f_a; r_c, t_c)\}, \tag{25}$$

where f_a is the azimuth frequency. Expanding the phase term in (25) into a Taylor series of f_a at $f_a = 0$, we have

$$\begin{aligned}\varphi_0(f_a; r_c, t_c) = {} & \phi_0(r_c, t_c) + \phi_1(r_c, t_c) f_a \\ & + \phi_2(r_c, t_c) f_a^2 + \phi_3(r_c, t_c) f_a^3 + \cdots\end{aligned} \tag{26}$$

where

$$\begin{cases} \phi_0(r_c, t_c) = -\dfrac{2\pi f_c (Z_0 - A_0 t_c)}{c}, & \phi_1(t_c) = -2\pi t_c \\ \phi_2(t_c) = \dfrac{\pi c}{B_0 f_c} = -\dfrac{\pi}{K_a}, & \phi_3(t_c) = \dfrac{\pi C_0 c^2}{3 B_0^3 f_c^2} \end{cases} \tag{27}$$

In (26), ϕ_0 and ϕ_1 are the constant and azimuth position terms, respectively; ϕ_2 reflects the azimuth modulation, which is essential for azimuth focusing, and ϕ_3 denotes the high-order term. The Doppler FM rate K_a can be expressed as

$$K_a = -\frac{B_0 f_c}{c} = -\frac{v^2 \cos^2(\theta_R)}{\lambda r_{\text{Rc}}}. \tag{28}$$

Inspecting (28), the Doppler FM rate is determined by the slant range at the beam center crossing time, r_{Rc}. According to (22), however, the slant ranges of echoes in a same range cell after RCMC are different, and so are the Doppler FM rates, which must be equalized before azimuth compression. The detailed derivation of equalization will be discussed in Section 4.

3.3 Algorithm validation

To validate the effectiveness of the range processing mentioned above, analyses on the bistatic range histories of the echoes after deramp operation, KT, and bulk RCMC are performed based on BiSAR parameters in Table 1, respectively. We assume five targets placed at the iso-range line of $R_{\text{total}}(0; r_c, t_c)$ in the coordinate plane, and the azimuth interval between them is 550 m.

Based on (5) and (14), Fig. 5 gives the bistatic range histories of the echoes before and after deramp operation, respectively. Due to the fact that the linear RCM component takes the dominant part of the total RCM, ramped bistatic range histories of the original echoes appear in Fig. 5a. While deramp operation has been performed, the ramps are removed, but large residual RCMs still exist as can be seen in Fig. 5b. For instance, the residual RCM at the edge in azimuth is about 4.0 m which cannot be neglected. In addition, the differences among the range curves of the five targets are still very large, so large migration errors will occur if a bulk RCMC operation is directly applied.

According to (14), the residual RCM contains residual linear and high-order components, where the residual

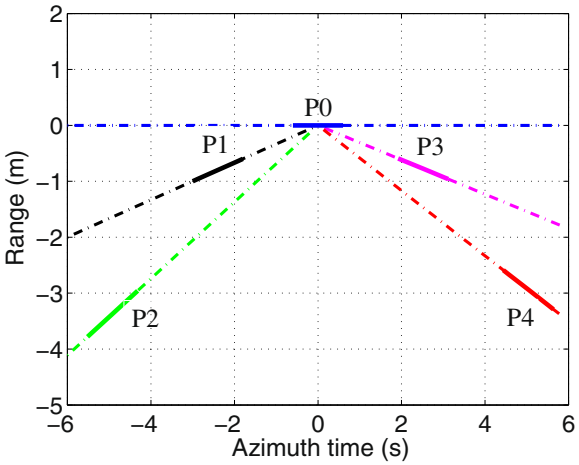

Fig. 6 Residual linear RCMs of the echoes after deramp operation

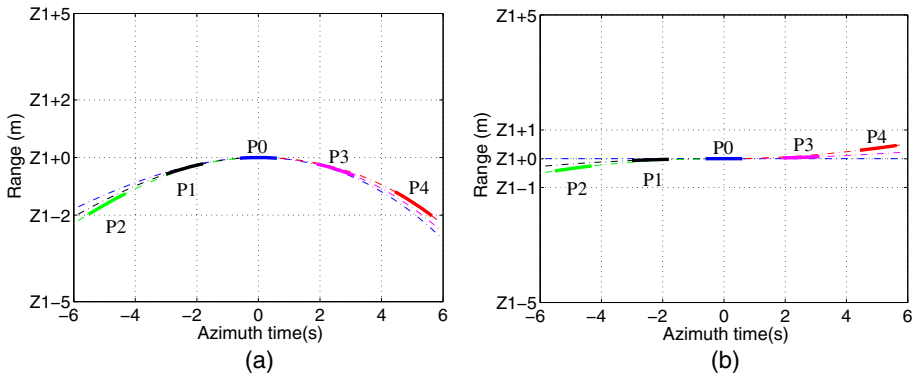

Fig. 7 Bistatic range histories of the echoes. **a** After KT. **b** After bulk RCMC

linear RCMs of the echoes are shown in Fig. 6. From the result, it is easy to find that the residual linear RCM of the target at azimuthal edge is over 3.0 m, which is larger than one range cell and should be removed.

Based on (18), the bistatic range histories of the echoes after KT are presented in Fig. 7a. Obviously, after fully removing the linear RCM, the remained new high-order RCM of the edge target in azimuth is about 4.0 m, but the differences among the range curves of the five targets are extremely small, which implies that it is suitable to apply a bulk RCMC. The bistatic range histories of the echoes after bulk RCMC are given in Fig. 7b. Comparing Fig. 7b with Fig. 5b, the result after bulk RCMC is much better than that after deramp operation. For instance, the migration error of the edge target in azimuth is only about 0.4 m, which is much smaller than one range cell and fully meets the requirement of high-squint one-stationary BiSAR configuration.

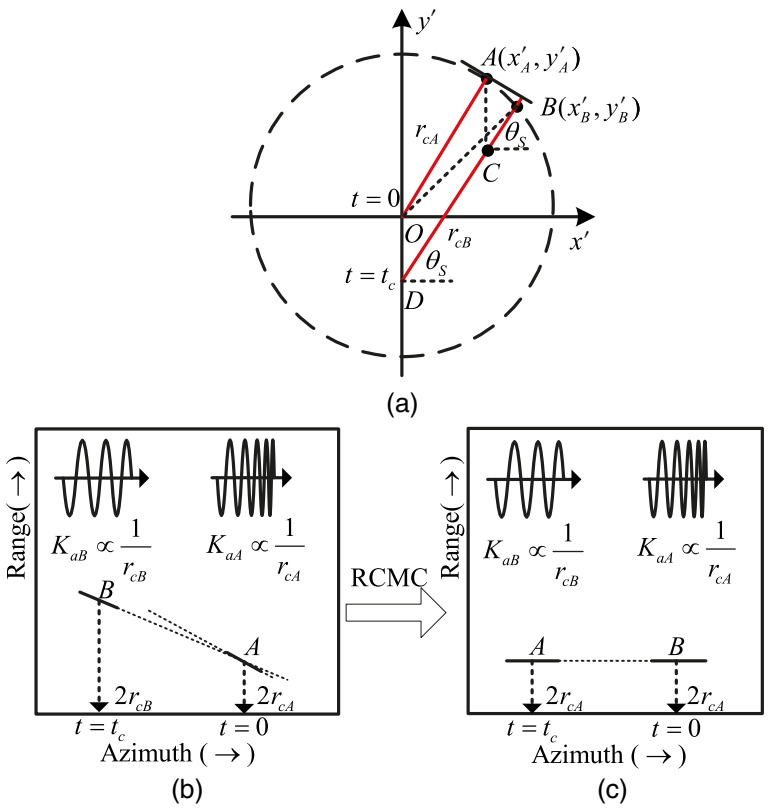

Fig. 8 **a** *Circle space*. *A* and *B* lie on the *circle* when they share the same $R_{\text{total}}(0; r_c, t_c)$. **b** Data space before RCMC. **c** Data space after RCMC. Range histories of *A* and *B* have been shifted into a same range cell

4 Enhanced azimuth NLCS algorithm

According to (28), the effectiveness of azimuth NLCS for BiSAR data is determined by the azimuth model of slant ranges at the beam center crossing time. However, the azimuth model of monostatic SAR is directly applied to focus BiSAR data in [20], which makes the imaging algorithm suffer limitations of applicability, especially when the baseline between the transmitter and the receiver is large.

In this section, we first analyze the azimuth dependency of slant ranges for monostatic SAR by a circle model. Then, an ellipse model is established to reveal the azimuth-variant characteristic of slant ranges for BiSAR. Based on the new model, coefficients of enhanced azimuth NLCS are derived to focus one-stationary BiSAR data. At last, the processing errors and limitations of scene size in azimuth of the new algorithm are both analyzed.

4.1 Circle model for monostatic SAR

In the monostatic SAR, targets with a same $R_{\text{total}}(0; r_c, t_c)$ in the coordinate plane can be seen that they lie on a circle with the center at the location of platform at $t = 0$. To simplify the analysis and derivation procedure, we assume that the space plane determined by the transmitter, the receiver, and the point target is mapped onto a new ground x'-y' plane. As seen in Fig. 8a, A and B denote two point targets with the same $R_{\text{total}}(0; r_c, t_c)$, where A is located at the azimuth center and it is chosen as the reference target and r_{cA} and r_{cB} are the slant ranges at their own beam center crossing time, respectively.

In the data space, the slant ranges of A and B are different and so are their Doppler FM rates according to (28), as seen in Fig. 8b. After RCMC, their range histories have been shifted into a same range cell, but their Doppler FM rates are still dependent on r_{cA} and r_{cB}, respectively, as seen in Fig. 8c. Therefore, we have to figure out the relationship between r_{cA} and r_{cB}, which is the key to azimuth NLCS processing.

Based on the circle model shown in Fig. 8a and after a series of geometry derivation, we obtain

$$r_{cB} = r_{DC} + r_{CB} \approx r_{cA} - v \sin(\theta_S)\, t_c = r_{cA} + A_0 t_c, \qquad (29)$$

when target B lies close to the reference target A.

It is obvious that the derived result in (29) is exactly the same as the original derivation result for monostatic SAR in [19], which validates the accuracy of our established circle model.

4.2 Ellipse model for one-stationary BiSAR

In BiSAR configuration, owing to the separation of the transmitter and the receiver, the circle model aforementioned

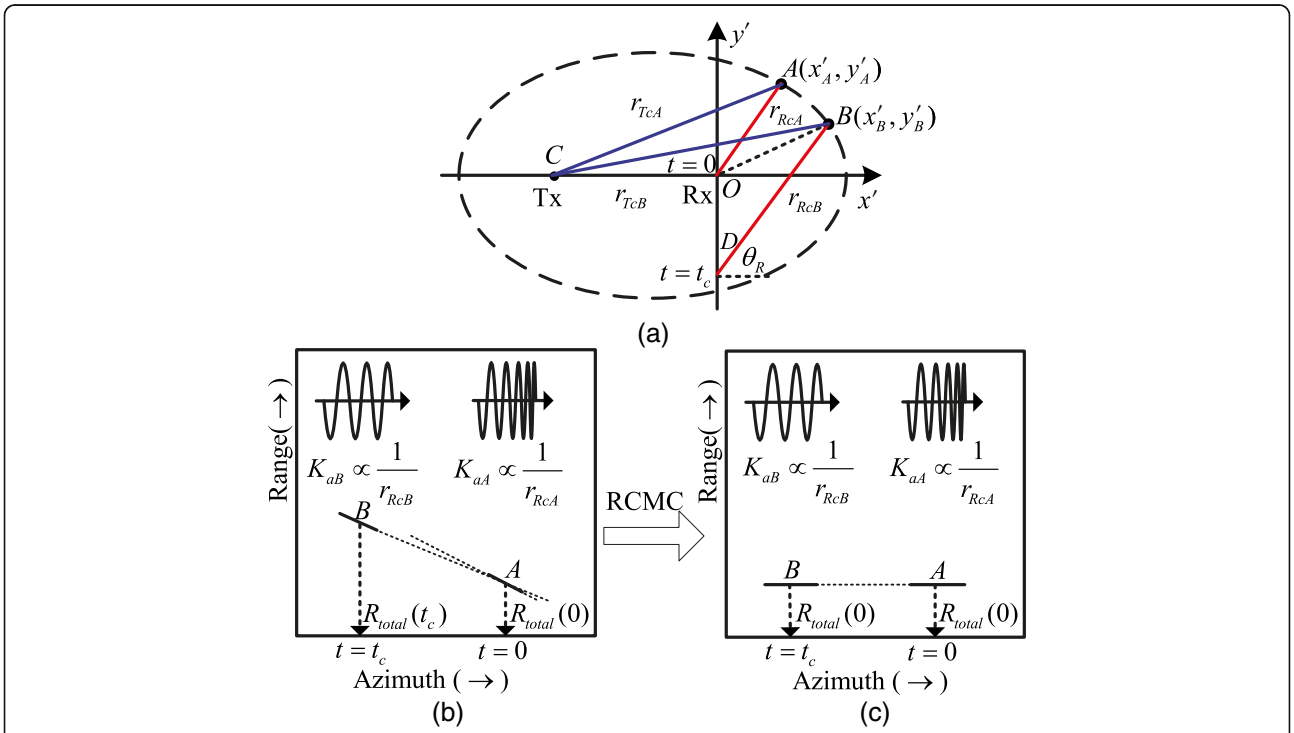

Fig. 9 **a** *Ellipse space*. *A* and *B* lie on the *ellipse* when they share the same $R_{\text{total}}(0; r_c, t_c)$. **b** Data space before RCMC. **c** Data space after RCMC. Range histories of *A* and *B* have been shifted into a same range cell

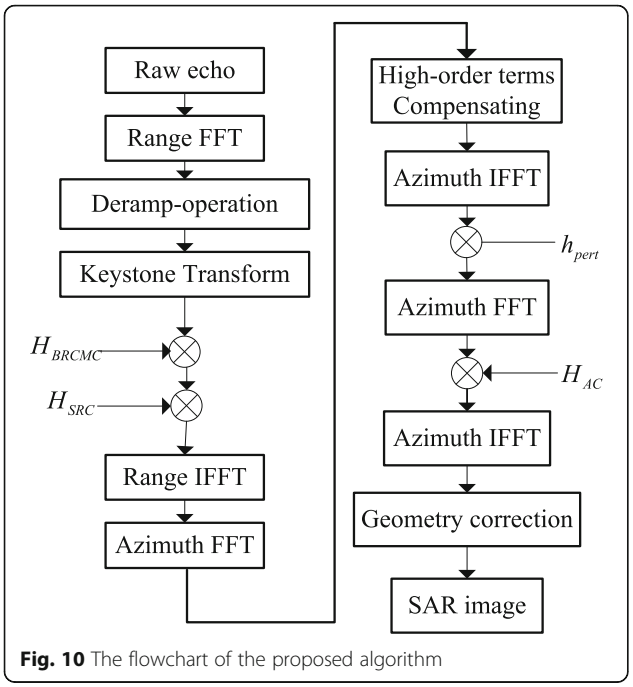

Fig. 10 The flowchart of the proposed algorithm

does not hold anymore. Thus, to reveal the azimuth-variant characteristic of Doppler FM rate for BiSAR, a new azimuth geometric model should be established.

Due to a two-different-way slant range in BiSAR, targets with the same $R_{\text{total}}(0; r_c, t_c)$ can be seen that they lie on an ellipse with the locations of platforms at $t = 0$ as the two foci (assuming that the stationary transmitter lies right above the x'-axis), as given in Fig. 9a. Targets A and B on the ellipse after RCMC have the relationship as follow

$$R_{\text{total}}(0; r_c, t_c) = r_{TcB} + r_{OB} = r_{TcA} + r_{RcA}. \tag{30}$$

where r_{OB} is distance from coordinate origin O to the target B, which implies the slant range of target B after RCMC operations.

At the same time, due to different lengths of r_{RcA} and r_{RcB}, the Doppler FM rates of targets A and B are different as seen in Fig. 9c. Therefore, the key step is to build the relationship between r_{RcB} and r_{RcA} for BiSAR case. Based on the established geometry in Fig. 9a, an equation of the ellipse can be expressed as

$$\frac{(x' + c)^2}{a^2} + \frac{y'^2}{a^2 - c^2} = 1, \tag{31}$$

where a denotes semi-major axis of the ellipse and c implies half of the bistatic baseline range L_{OC}, and given by

$$a = \frac{r_{RcA} + r_{TcA}}{2}, \quad c = \frac{L_{OC}}{2}. \tag{32}$$

Combining (30) with (31), the relationship between r_{RcB} and r_{RcA} can be resolved,

$$r_{RcB} \approx r_{RcA} + r_{RcA} \frac{A_0}{a(1-e^2)} t_c \tag{33}$$

where $e = c/a$ is the eccentricity of the ellipse. It is obvious that (29) is a special case of (33) when the eccentricity e is set to zero and a equals to r_{RcA}, which means that the ellipse model degrades to a circle model.

Notice that the derived result in [20] for BiSAR is exactly the same as in (29) for monostatic SAR, which means that the monostatic model is directly applied to BiSAR case in [20]. This will result in severe azimuth processing error, especially when focusing large-baseline BiSAR data.

4.3 Azimuth equalization and compression operation

In this subsection, we derive an enhanced azimuth NLCS to focus one-stationary BiSAR data based on the result of the ellipse model established in Section 4.2.

According to (28) and (33), the Doppler FM rate of target B can be expressed as

$$\begin{aligned} K_{aB} &= -\frac{v^2 \cos^2(\theta_R)}{\lambda r_{RcB}} \\ &= -\frac{v^2 \cos^2(\theta_R)}{\lambda \left(r_{RcA} + r_{RcA} \frac{A_0}{a(1-e^2)} t_c \right)} \end{aligned} \tag{34}$$

Expanding (34) into a Taylor series of t_c at $t_c = 0$, we have

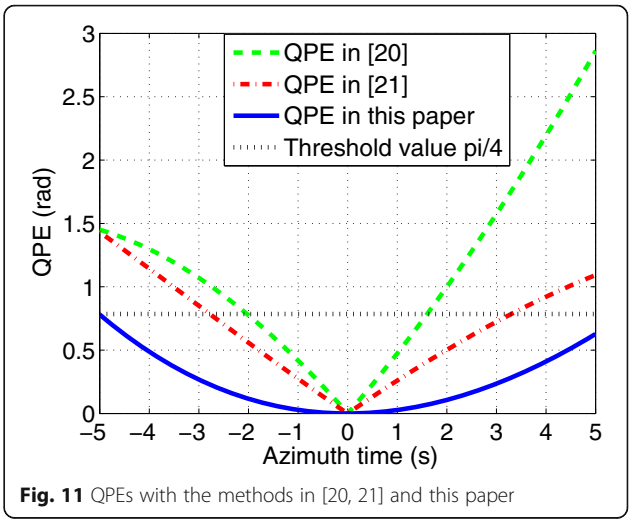

Fig. 11 QPEs with the methods in [20, 21] and this paper

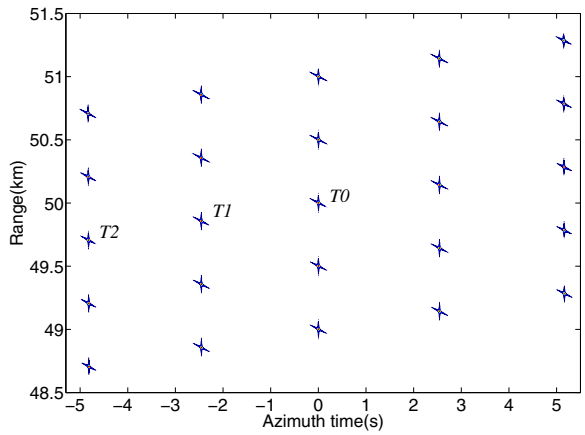

Fig. 12 Entire focused images by the proposed algorithm in case I

$$K_{aB} \approx \frac{-v^2\cos^2(\theta_R)}{\lambda r_{RcA}} + \frac{A_0 v^2\cos^2(\theta_R)}{\lambda r_{RcA} a(1-e^2)} \cdot t_c = K_{aA} + K_s t_c, \tag{35}$$

where K_{aA} is the Doppler FM rate of the reference target A, and K_s is the coefficient of azimuth-variant component of the Doppler FM rate.

Inspecting (26), due to the minor impact of the high-order term ϕ_3 in high-squint BiSAR, it can be simply compensated by multiplying its conjugate. Then, transforming the signal of target B back to azimuth time domain using PSP, we obtain

$$s_B(t_m; t_c) = exp\{j\phi_B(t_m, t_c)\}, \tag{36}$$

where

$$\phi_B(t_m; t_c) = \pi K_{aB}(t_m - t_c)^2. \tag{37}$$

To equalize the Doppler FM rates of targets A and B, a perturbation function of cubic form is defined by

$$h_{\text{pert}}(t_m) = exp\{j\pi p t_m^3\}, \tag{38}$$

where the parameter p is the coefficient of the perturbation function.

Setting $t_p = t_m - t_c$ and multiplying (38) with (36), the phase term of the azimuth signal of target B is

$$\phi_{B\text{pert}}(t_p) = \pi p t_c^3 + 3\pi p t_c^2 t_p + \left(3\pi p t_c - \frac{\pi v^2\cos^2(\theta_R)}{\lambda r_{RcA}} + \frac{\pi A_0 v^2\cos^2(\theta_R)}{\lambda r_{RcA} a(1-e^2)} t_c\right) t_p^2 + \pi p t_p^3 \tag{39}$$

To find the coefficient p, the sum of the quadratic terms of t_p that involve the target azimuth position parameter t_c is set to zero, and then, we have

$$p = -\frac{A_0 v^2\cos^2(\theta_R)}{3a(1-e^2)\lambda r_{RcA}} = -\frac{K_s}{3}. \tag{40}$$

Then, substituting (40) into (39), the phase term of azimuth signal of target B becomes

$$\phi_{B\text{pert}}'(t_p) = \frac{\pi v^2\cos^2(\theta_R)}{3a(-1+e^2)\lambda r_{RcA}}\left\{A_0 t_c^3 + 3A_0 t_c^2 t_p + 3a(1-e^2)t_p^2 + A_0 t_p^3\right\}. \tag{41}$$

Ignoring the constant term of (41) and performing a Fourier transform using PSP and then the azimuth frequency is related to the azimuth time by

$$2\pi f_a = k_1 t_p + k_2 t_p^2, \tag{42}$$

where

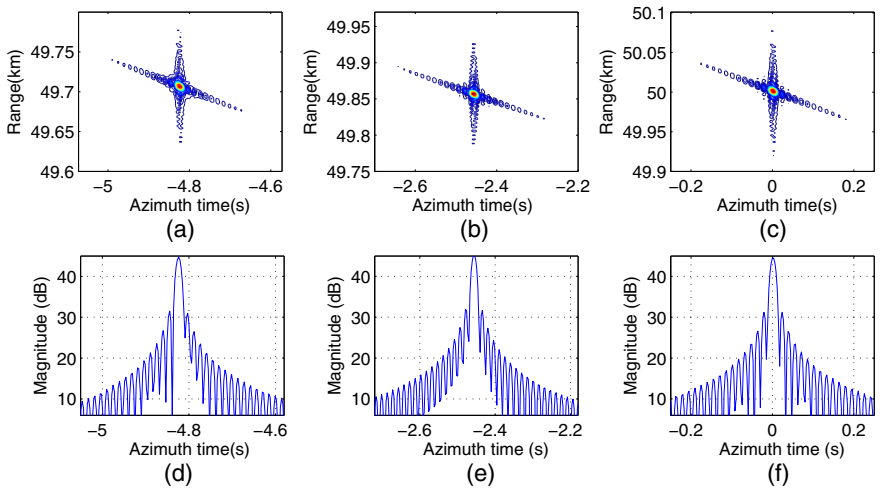

Fig. 13 Results by the traditional algorithm in [20] in case I. **a** Focused image of T_2. **b** Focused image of T_1. **c** Focused image of T_0. **d** Azimuth profile of T_2. **e** Azimuth profile of T_1. **f** Azimuth profile of T_0

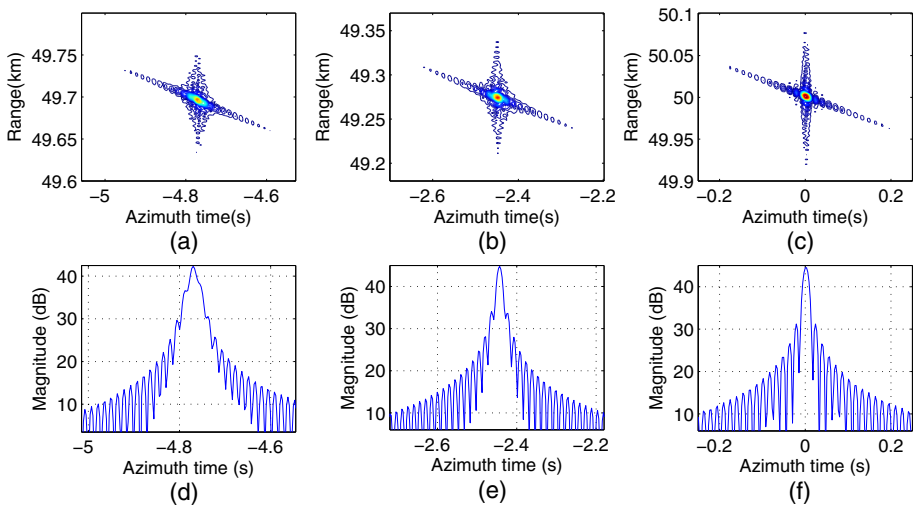

Fig. 14 Results by the proposed algorithm in case I. **a** Focused image of T_2. **b** Focused image of T_1. **c** Focused image of T_0. **d** Azimuth profile of T_2. **e** Azimuth profile of T_1. **f** Azimuth profile of T_0

$$k_1 = 2\pi K_{aA}, \quad k_2 = -\pi K_s \tag{43}$$

Using the method of series reversion (MSR) [22], we can obtain

$$t_p(f_a) = K_1 f_a + K_2 f_a^2, \tag{44}$$

where

$$K_1 = \frac{1}{k_1}, \quad K_2 = -\frac{k_2}{k_1^3}. \tag{45}$$

Substituting (44) into (42), we have

$$\phi(f_a) \approx S_0 + S_1 f_a + S_2 f_a^2 + S_3 f_a^3, \tag{46}$$

where

$$\begin{cases} S_0 = -\dfrac{\pi K_s t_c^3}{3}, & S_1 = -2\pi t_c \\ S_2 = -\dfrac{\pi}{K_{aA}}, & S_3 = -\dfrac{\pi K_s}{3K_{aA}^3} \end{cases} \tag{47}$$

Thus, the azimuth compression filtering function can be constructed as

$$H_{AC}(f_a) = exp\{-j(S_2 f_a^2 + S_3 f_a^3)\}. \tag{48}$$

Table 2 Performance parameters in azimuth for case I

Performance parameters		T_2	T_1	T_0
Traditional algorithm in [20]	PSLR(dB)	6.52	9.69	13.27
	ISLR(dB)	5.32	6.62	9.99
Proposed algorithm in this paper	PSLR(dB)	13.13	13.26	13.29
	ISLR(dB)	9.95	9.98	9.99

Figure 10 shows the flowchart of the proposed algorithm in this paper.

4.4 QPE and scene size analysis

Inspecting (34), the first-order expansion is adopted to approximate the Doppler FM rate, and this will cause an inevitable error along azimuth direction which is called the quadratic phase error (QPE). In this subsection, the QPEs along azimuth direction based on the expressions of Doppler FM rate in (34), [20, 21] are analyzed, respectively.

The QPE caused by the first-order approximation of the Doppler FM rate in (34) can be expressed as

$$QPE = \pi |K_{aB} - (K_{aA} + K_s t_c)| \left(\frac{T_a}{2}\right)^2, \tag{49}$$

which should not exceed the threshold value $\pi/4$ for the validity of azimuth NLCS.

Table 3 Stationary parameters of BiSAR for case II

Simulation parameters	Transmitter	Receiver
Velocity		50 m/s
Beam center slant range	6.88 km	3.12 km
Squint angle		30°
Altitude	0.5 km	1.0 km
Pulse repetition frequency	120 Hz	
Carrier frequency	10.0 GHz	
Range bandwidth	214.3 MHz	
Synthetic aperture time	3.56 s	
Bistatic bsaeline range	4 km	

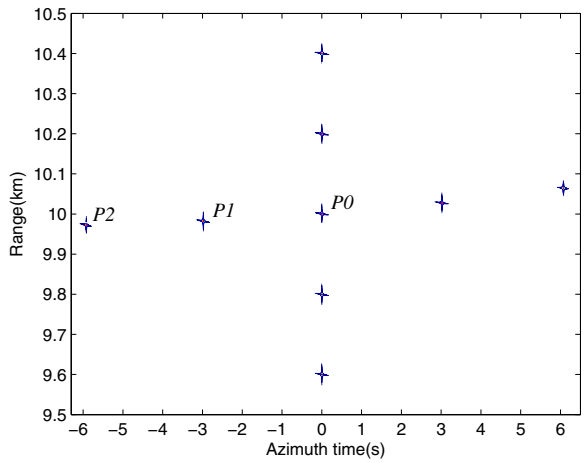

Fig. 15 Entire focused images by the proposed algorithm in case II

Based on simulation parameters in Table 1, Fig. 11 gives the QPEs along azimuth direction using (49) and that of the methods in [20, 21], respectively. It is easy to find that the QPE in (49) is kept under $\pi/4$ within the entire azimuth scene, while the QPEs with the methods in [20, 21] are both much larger than $\pi/4$ at the edge in azimuth. This means that a much larger azimuth scene can be processed by the enhanced azimuth NLCS proposed in this paper than the methods in [20, 21].

5 Simulation results

To demonstrate the effectiveness of the enhanced azimuth NLCS algorithm proposed by this paper, two experiments with simulated data are carried out in this section. Both the two simulations involve airborne configurations. The first simulation is carried out with a typical airplane self-navigation configuration, which processes a relatively large imaging scene. The second one is operated with an airplane self-landing configuration, which involves high resolutions in both range and azimuth.

Case I: the imaging scene is set to be 2.0 km in range and 2.2 km in azimuth, and this simulation chooses an array of 5×5 point targets with an interval of 500.0 m in range and 550.0 m in azimuth. The theoretical range resolution is 2.0 m, and the azimuth resolution is 1.7 m. The simulation parameters for this experiment are listed in Table 1.

The focused images processed by the enhanced NLCS algorithm are shown in Fig. 12. From the results, it can be seen that all the targets in the imaging scene are focused well, where T_0 is the scene center and T_2 represents the edge target in azimuth in the imaging scene. In order to evaluate the focusing performance, the sub-contour images of these three targets, which are processed by the method in [20], and the enhanced NLCS algorithm in this paper, respectively, are shown in Figs. 13 and 14, and their corresponding deskewed azimuth profiles give a more detailed comparison of the focused results. With the method in [20], the imaging quality deteriorates as the distance increases in azimuth from target to scene center. This is due to that the QPEs by the traditional NLCS of [20] become large for the whole scene. With the enhanced NLCS algorithm proposed by this paper, however, even the target located at azimuth edge is focused well. In addition, the performance parameters of the point targets of the two algorithms are given in Table 2, which further verifies the effectiveness of the algorithm proposed by this paper.

Case II: the theoretical resolutions in both range and azimuth are 0.7 m. The imaging scene is set to be 800.0 m in range and 600.0 m in azimuth, and this simulation uses an array of nine targets, which are laid out

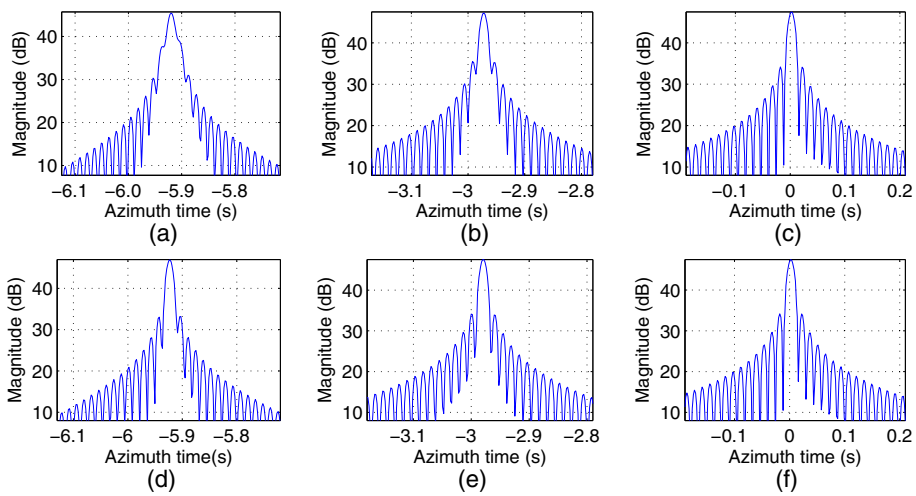

Fig. 16 Azimuth profiles of the three targets by different algorithms in case II. **a** P_2, **b** P_1, and **c** P_0 by traditional algorithm in [20]. **d** P_2, **e** P_1, and **f** P_0 by the proposed algorithm in this paper

Table 4 Performance parameters in azimuth for case II

Performance parameters		P_2	P_1	P_0
Traditional algorithm in [20]	PSLR(dB)	6.84	10.77	13.28
	ISLR(dB)	5.56	7.56	9.99
Proposed algorithm in this paper	PSLR(dB)	13.21	13.27	13.29
	ISLR(dB)	9.81	9.94	9.99

on a rectangular grid with an interval of 200.0 m in range and 150.0 m in azimuth. The simulation parameters for this experiment are listed in Table 3.

Figure 15 shows the entire focused images processed by the enhanced NLCS algorithm in this paper. Observing the results, all the targets are focused well, where P_0 is the scene center and P_2 represents the edge target in azimuth in the imaging scene. In addition, the deskewed azimuth profiles of targets P_0, P_1, and P_2 processed by the method in [20] and the enhanced NLCS algorithm in this paper are displayed in Fig. 16, and their corresponding performance parameters are listed in Table 4. The results of this simulation further verify the effectiveness of the algorithm proposed by this paper.

6 Conclusions

This paper proposes an enhanced azimuth NLCS algorithm based on an ellipse model to focus one-stationary BiSAR data with high-squint, large-baseline configuration. In the range processing, a method combining deramp operation and KT is adopted to remove linear RCM completely and mitigate range-azimuth cross-coupling. After that, an ellipse model is proposed to analyze the azimuth-variant characteristic of Doppler phase of one-stationary BiSAR data. Based on the new model, an enhanced azimuth NLCS is derived to handle one-stationary BiSAR data. Compared with the traditional algorithm, better imaging performance can be achieved by the proposed algorithm in this paper. Additionally, the ellipse model and the enhanced NLCS algorithm proposed by this paper also show potential for other bistatic cases like BiSAR with nonparallel tracks, forward-looking BiSAR, and even general BiSAR.

Acknowledgements
The authors would like to thank all the anonymous reviewers for their hard work.

Funding
This work was supported by the National Natural Science Foundation of China (61301248, 61271214), and by the Chinese Innovation Foundation of Aerospace Science and Technology.

Authors' contributions
HZ and SZ conceived and designed the research. HZ, SZ, and JH performed the experiments. HZ and SZ wrote the manuscript. HZ, SZ, and MS reviewed and edited the manuscript. All authors read and approved the manuscript.

Competing interests
The authors declare that they have no competing interests.

Publisher's Note

Received: 16 December 2016 Accepted: 24 April 2017
Published online: 08 May 2017

References

1. M Rodriguez-Cassola, SV Baumgartner, G Krieger, and A Moreira, Bistatic TerraSAR-X/F-SAR spaceborne-ariborne SAR experiment: Description, data processing, and results. IEEE Trans Geosci Remote Sens **48**(2), 781–794 (2010)
2. SC Chen, MD Xing, S Zhou, L. Zhang, and Z. Bao, Focusing of tandem bistatic SAR data using the chirp-scaling algorithm. EURASIP J. Adv. Signal Process **38**, 1–13 (2013)
3. W Pu, YL. Huang, JJ. Wu, J. Y. Yang, and W C. Li, A residual range cell migration correction algorithm for bistatic forward-looking SAR. EURASIP J. Adv. Signal Process **110**, 1–12 (2016)
4. R Wang et al., Processing the azimuth-variant bistatic SAR data by using monostatic imaging algorithms based on 2-D principle of stationary phase. IEEE Trans Geosci Remote Sens **49**(10), 3504–3520 (2011)
5. L Maslikowsli, P Samczynski, M Baczyk, P Krysik, K Kulpa, Passive bistatic SAR imaging: challenges and limitations. IEEE Trans Aerosp Electron Syst **29**(7), 23–29 (2014)
6. R Wang et al., Double-channel bistatic SAR system with spaceborne illuminater for 2-D and 3-D SAR remote sensing. IEEE Trans Geosci Remote Sens **51**(8), 4496–4570 (2013)
7. T Zeng, R Wang, F Li, T Long, A modified nonlinear chirp scaling algorithm for spaceborne/stationary bistatic SAR based on series reversion. IEEE Trans Geosci Remote Sens **51**(5), 3108–3118 (2013)
8. G Krieger, A Moreira, Spaceborne bi- and multistatic SAR: potential and challenges. IET Radar Sonar Navigat **153**(3), 184–198 (2006)
9. A Renga, A Moccia, Performance of stereoradargrammetric mothods applied to spaceborne monostatic-bistatic synthetic aperture radar. IEEE Trans Geosci Remote Sens **47**(2), 544–560 (2009)
10. XL Qiu, DH Hu, CB Ding, An improved NLCS algorithm with capability analysis for one-stationary bistatic SAR. IEEE Trans Geosci Remote Sens **46**(10), 3179–3186 (2008)
11. T Zeng, C Hu, LX Wu, FF Liu, WM Tian, M Zhu, T Long, Extended NLCS algorithm of BiSAR systems with a squinted transmitter and a fixed receiver: theory and experimental confirmation. IEEE Trans Geosci Remote Sens **51**(10), 5019–5030 (2013)
12. ZY Li, JJ Wu, WC Li, YL Huang, JL Yang, One-stationary bistatic side-looking SAR imaginmg algorithm based on extended keystone transforms and nonlinear chirp scaling. IEEE Geosci Remote Sens Lett **10**(2), 211–215 (2013)
13. X L Qiu, F Behner, S Reuter, H Nies, O Loffeld, L J Huang, D H Hu, and C B Ding. An imaging algorithm based on keystone transform for one-stationary bistatic SAR of spolight model. EURASIP J. Adv. Signal Process **221**, 1–11 (2012).
14. JJ Wu, ZY Li, YL Huang, JY Yang, HG Yang, QH Liu, Focusing bistatic forward-looking SAR with stationary transmitter based on keystone transform and nonlinear chirp scaling. IEEE Geosci Remote Sens Lett **11**(1), 148–152 (2014)
15. K Natroshvili, O Loffeld, H Nies, AM Ortiz, S Knedlik, Focusing of general bistatic SAR configuration data with 2-D inverse scaled FFT. IEEE Trans Geosci Remote Sens **44**(10), 2718–2727 (2006)
16. J Wu, Z Li, Y Huang, QH Liu, J Yang, Processing one-stationary bistatic SAR data using inverse scaled fourier transform. Prog Electromagn Res **129**, 143–159 (2012)
17. HS Shin, JT Lim, Omega-k algorithm for airborne forward-looking bistatic spotlight SAR imaging. IEEE Geosci Remote Sens Lett **6**(2), 312–316 (2009)
18. JJ Wu, ZY Li, YL Huang, JY Yang, QH Liu, Omega-k imaging algorithm for one-stationary bistatic SAR. IEEE Trans Aerosp Electron Syst **4**(1), 33–52 (2014)
19. FH Wong, T Yeo, New application of nonlinear chirp scaling in SAR data processing. IEEE Trans Geosci Remote Sens **39**(5), 946–953 (2001)
20. FH Wong, IG Cumming, YL Neo, Focusing bistatic SAR data using the nonlinear chirp scaling algorithm. IEEE Trans Geosci Remote Sens **46**(9), 2493–2505 (2008)
21. D Li, GS Liao, W Wang, Q Xu, Extended azimuth nonlinear chirp scaling algorithm for BSAR processing in high-resolution highly squinted model. IEEE Geosci Remote Sens **11**(6), 1134–1138 (2014)
22. Y Neo, F Wong, IG Gumming, A two-dimensional spectrum for bistatic SAR processing using series reversion. IEEE Geosci Remote Sens Lett **4**(1), 93–96 (2007)